Constraints on Solar Reflected Dark Matter from a combined analysis of XENON1T and XENONnT data

E. Aprile [1], J. Aalbers [2], K. Abe [3], M. Adrover [4], S. Ahmed Maouloud [5], L. Althueser [6], B. Andrieu [5], E. Angelino [7], D. Antón Martin [8], S. R. Armbruster [9], F. Arneodo [10], L. Baudis [4], M. Bazyk [11], L. Bellagamba [12], R. Biondi [7], A. Bismark [4], K. Boese [9], R. M. Braun [6], G. Bruni [12], G. Bruno [11], R. Budnik [13], C. Cai,[14] C. Capelli [4], J. M. R. Cardoso [15], A. P. Cimental Chávez [4], A. P. Colijn [16], J. Conrad [17, *], J. J. Cuenca-García [4], V. D'Andrea [7, †], L. C. Daniel Garcia [5], M. P. Decowski [16], A. Deisting [18], C. Di Donato [19, 7], P. Di Gangi [12], S. Diglio [11], K. Eitel [20], S. el Morabit [16], R. Elleboro,[19] A. Elykov [20], A. D. Ferella [19, 7], C. Ferrari [7], H. Fischer [21], T. Flehmke [17], M. Flierman [16], R. Frankel [13], D. Fuchs [17], W. Fulgione [22, 7], C. Fuselli [16], R. Gaior [5], F. Gao [14], R. Giacomobono [23], F. Girard [5], R. Glade-Beucke [21], L. Grandi [8], J. Grigat [21], H. Guan [24], M. Guida [9], P. Gyorgy [18], R. Hammann [9], A. Higuera [25], C. Hils [18], L. Hoetzsch [4], N. F. Hood [26], M. Iacovacci [23], Y. Itow [27], J. Jakob [6], F. Joerg [4], Y. Kaminaga [3], M. Kara [20], S. Kazama [27], P. Kharbanda [16], M. Kobayashi [27], D. Koke [6], K. Kooshkjalali,[18] A. Kopec [26, ‡], H. Landsman [13], R. F. Lang [24], L. Levinson [13], I. Li [25], S. Li [28], S. Liang [25], Z. Liang [28], Y.-T. Lin [9, 6], S. Lindemann [21], M. Lindner [9], K. Liu [14], M. Liu [1], J. Loizeau [11], F. Lombardi [18], J. A. M. Lopes [15, §], G. M. Lucchetti [12], T. Luce [21], Y. Ma [26], C. Macolino [19, 7], J. Mahlstedt [17], F. Marignetti [23], T. Marrodán Undagoitia [9], K. Martens [3], J. Masbou [11], S. Mastroianni [23], V. Mazza [12], A. Melchiorre [19, 7], J. Merz [18], M. Messina [7], A. J. P. Michel [20], K. Miuchi [29], A. Molinario [22], S. Moriyama [3], K. Morå [1], M. Murra [1], J. Müller [21], K. Ni [26], C. T. Oba Ishikawa [3], U. Oberlack [18], S. Ouahada [4], B. Paetsch [13], Y. Pan [5], Q. Pellegrini [5], R. Peres [4], J. Pienaar [13], M. Pierre [16], G. Plante [1], T. R. Pollmann [16], A. Prajapati [19], L. Principe [11], J. Qin [25], D. Ramírez García [4], A. Ravindran [11], A. Razeto [7], R. Singh [24], L. Sanchez [25], J. M. F. dos Santos [15], I. Sarnoff [10], G. Sartorelli [12], J. Schreiner,[9] P. Schulte [6], H. Schulze Eißing [6], M. Schumann [21], L. Scotto Lavina [5], M. Selvi [12], F. Semeria [12], F. N. Semler [21], P. Shagin [18], S. Shi [1], H. Simgen [9], Z. Song [30], A. Stevens [21], C. Szyszka [18], A. Takeda [3], Y. Takeuchi [29], P.-L. Tan [1, ¶], D. Thers [11], G. Trinchero [22], C. D. Tunnell [25], K. Valerius [20], S. Vecchi [31], S. Vetter [20], G. Volta [9], C. Weinheimer [6], M. Weiss [13], D. Wenz [6], C. Wittweg [4], V. H. S. Wu [20], Y. Xing [11], D. Xu [1], Z. Xu [1], M. Yamashita [3], J. Yang [28], L. Yang [26], J. Ye [30], M. Yoshida [3], L. Yuan [8], G. Zavattini [31], Y. Zhao [14], M. Zhong [26], and T. Zhu [3]

(XENON Collaboration)[**]

[1] *Physics Department, Columbia University, New York, NY 10027, USA*
[2] *Nikhef and the University of Groningen, Van Swinderen Institute, 9747AG Groningen, Netherlands*
[3] *Kamioka Observatory, Institute for Cosmic Ray Research, and Kavli Institute for the Physics and Mathematics of the Universe (WPI), University of Tokyo, Higashi-Mozumi, Kamioka, Hida, Gifu 506-1205, Japan*
[4] *Physik-Institut, University of Zürich, 8057 Zürich, Switzerland*
[5] *LPNHE, Sorbonne Université, CNRS/IN2P3, 75005 Paris, France*
[6] *Institut für Kernphysik, University of Münster, 48149 Münster, Germany*
[7] *INFN-Laboratori Nazionali del Gran Sasso and Gran Sasso Science Institute, 67100 L'Aquila, Italy*
[8] *Department of Physics, Enrico Fermi Institute & Kavli Institute for Cosmological Physics, University of Chicago, Chicago, IL 60637, USA*
[9] *Max-Planck-Institut für Kernphysik, 69117 Heidelberg, Germany*
[10] *New York University Abu Dhabi - Center for Astro, Particle and Planetary Physics, Abu Dhabi, United Arab Emirates*
[11] *SUBATECH, IMT Atlantique, CNRS/IN2P3, Nantes Université, Nantes 44307, France*
[12] *Department of Physics and Astronomy, University of Bologna and INFN-Bologna, 40126 Bologna, Italy*
[13] *Department of Particle Physics and Astrophysics, Weizmann Institute of Science, Rehovot 7610001, Israel*
[14] *Department of Physics & Center for High Energy Physics, Tsinghua University, Beijing 100084, P.R. China*
[15] *LIBPhys, Department of Physics, University of Coimbra, 3004-516 Coimbra, Portugal*
[16] *Nikhef and the University of Amsterdam, Science Park, 1098XG Amsterdam, Netherlands*
[17] *Oskar Klein Centre, Department of Physics, Stockholm University, AlbaNova, Stockholm SE-10691, Sweden*
[18] *Institut für Physik & Exzellenzcluster PRISMA+, Johannes Gutenberg-Universität Mainz, 55099 Mainz, Germany*
[19] *Department of Physics and Chemistry, University of L'Aquila, 67100 L'Aquila, Italy*
[20] *Institute for Astroparticle Physics, Karlsruhe Institute of Technology, 76021 Karlsruhe, Germany*
[21] *Physikalisches Institut, Universität Freiburg, 79104 Freiburg, Germany*
[22] *INAF-Astrophysical Observatory of Torino, Department of Physics, University of Torino and INFN-Torino, 10125 Torino, Italy*
[23] *Department of Physics "Ettore Pancini", University of Napoli and INFN-Napoli, 80126 Napoli, Italy*

[24] *Department of Physics and Astronomy, Purdue University, West Lafayette, IN 47907, USA*
[25] *Department of Physics and Astronomy, Rice University, Houston, TX 77005, USA*
[26] *Department of Physics, University of California San Diego, La Jolla, CA 92093, USA*
[27] *Kobayashi-Maskawa Institute for the Origin of Particles and the Universe, and Institute for Space-Earth Environmental Research, Nagoya University, Furo-cho, Chikusa-ku, Nagoya, Aichi 464-8602, Japan*
[28] *Department of Physics, School of Science, Westlake University, Hangzhou 310030, P.R. China*
[29] *Department of Physics, Kobe University, Kobe, Hyogo 657-8501, Japan*
[30] *School of Science and Engineering, The Chinese University of Hong Kong (Shenzhen), Shenzhen, Guangdong, 518172, P.R. China*
[31] *INFN-Ferrara and Dip. di Fisica e Scienze della Terra, Università di Ferrara, 44122 Ferrara, Italy*

We report on a search for sub-GeV dark matter upscattered via the solar reflection mechanism in the heavy mediator scenario. Under the Standard Halo Model, keV to MeV dark matter produces nuclear recoils with energies below the detection threshold of liquid xenon time projection chambers. We enhance sensitivity to low-mass dark matter by considering dark matter-electron scattering, employing dedicated event selections to reduce the detection threshold, and exploiting the additional kinetic energy imparted to the dark matter particle by solar upscattering. Using XENON1T ionization-only and XENONnT low-energy electronic recoil datasets, we exclude previously unconstrained DM-electron scattering cross section for masses between $4.6\,\mathrm{keV}/c^2$ and $20\,\mathrm{keV}/c^2$, and between $0.2\,\mathrm{MeV}/c^2$ and $2\,\mathrm{MeV}/c^2$, reaching a minimum of $3.41 \times 10^{-39}\,\mathrm{cm}^2$ for a mass of $0.3\,\mathrm{MeV}/c^2$ at 90% confidence level.

Introduction — A wide range of astrophysical and cosmological observations point to the existence of dark matter (DM), a nonluminous component that dominates the matter content of the Universe. These observations are most naturally explained by one or more new particle species beyond the Standard Model [1]. Despite extensive searches, DM particles remain undetected [2]. Among direct detection efforts, liquid xenon time projection chambers (TPCs) currently place the most stringent limits on DM-nucleon interactions in the GeV–TeV mass range [3–5].

The XENONnT experiment, located at the INFN Laboratori Nazionali del Gran Sasso (LNGS), is the latest iteration of the multi-staged XENON program, succeeding XENON1T [6]. It consists of three nested detectors: a water Cherenkov muon veto [7], a water Cherenkov neutron veto to suppress radiogenic neutron background [8], and a double-walled cryostat containing 8.5 t of liquid xenon. Within the cryostat lies a dual-phase TPC with 5.9 t of instrumented liquid xenon in a cylindrical volume (1.49 m height, 1.33 m diameter) with a thin gaseous xenon layer on the liquid xenon [9, 10]. Several key systems, such as the cryogenic gas purification and krypton distillation column, were developed for XENON1T. Notable improvements in the XENONnT experiment include the liquid xenon purification [11] and high-flow radon removal systems [12].

When a particle interacts with xenon atoms in the TPC, it deposits energy, creating prompt scintillation photons and ionization electrons. The prompt scintillation photons are detected by the arrays of photomultiplier tubes (PMTs) at the top and bottom of the TPC, forming the prompt scintillation signal (S1) [13]. The electrons drift upwards under an electric field generated by the cathode at the bottom of the TPC and the gate electrode near the liquid surface. Upon reaching the liquid-gas interface, the electrons are extracted into the gaseous xenon by a stronger extraction field [10]. The accelerated electrons produce further electroluminescence in the gaseous xenon, resulting in the delayed ionization signal (S2) which is also detected by the PMT arrays [14].

In the Standard Halo Model (SHM), DM particles in the local galactic DM halo have speeds up to $\sim 800\,\mathrm{km/s}$ in the Earth's lab frame [15]. For sub-GeV DM, such velocities typically produce recoil energies below the detection thresholds of liquid xenon TPCs. These thresholds are 1 keV for combined scintillation and ionization signals [16] and 13.7 eV for the smallest ionization-only signals [17], restricting sensitivity to GeV–TeV and MeV masses respectively.

To extend the sensitivity to light DM, we make the following three analysis choices. First, we consider DM-electron scattering, which allows detection of lighter DM compared to DM-nucleus interactions. Second, we use specialized event selections considering ionization-only signals (S2-only) and low-energy electronic recoil (ER) signals to enhance sensitivity to smaller energy deposits. Finally, DM particles can gain kinetic energy by scattering with astrophysical targets [18–22]. We consider upscattering by the Sun [21, 22], which can reflect halo DM toward Earth with increased kinetic energy and hence higher detection efficiency.

In this work, we examine the upscattering of leptophilic sub-GeV DM particles in the galactic halo by electrons in the solar plasma, also known as solar-reflected dark matter (SRDM). We focus on the scenario in which the DM-electron interaction is mediated by a heavy particle, resulting in a contact interaction. The DM-electron cross section is constant with momentum transfer q, with DM form factor of $F_{\mathrm{DM}}(q) = 1$ [23]. The DM-electron interaction responsible for upscattering DM in the Sun is the same interaction that produces ER signals in the detec-

tor, so no additional coupling is assumed. Using data from the XENON1T S2-only [24] and XENONnT low-energy ER [16] analyses, we derive 90% confidence level (C.L.) confidence intervals on the DM-electron cross section for DM masses between $4.6 \, \mathrm{keV}/c^2$ and $9 \, \mathrm{MeV}/c^2$.

Solar Reflected Dark Matter — The final kinetic energy of an up-scattered DM particle has an analytic expression if the DM particle only scattered once in the solar plasma [21]. However, for many combinations of the DM mass and DM-electron cross section, multiple-scattering becomes significant. This renders the analytic treatment intractable and the SRDM differential flux must be evaluated numerically. In this work, we compute the SRDM differential flux using Monte Carlo simulations implemented in DaMaSCUS-SUN [25].

The computation of the SRDM flux follows the simulation procedure outlined in [23]. The process begins by sampling the initial position and velocity of DM particle falling into the Sun and propagating the particle through the solar interior. As the DM particle traverses the solar plasma, it may scatter off electrons according to the assumed DM-electron scattering cross section. During its passage, the DM particle may undergo one of three processes: traverse the Sun without scattering, become gravitationally captured through repeated interactions, or scatter at least once and escape, thus contributing to the SRDM population.

The probability of solar reflection is estimated as the fraction of simulated DM particles that scatter at least once and subsequently escape, relative to the total number of simulated trajectories. The reflected DM particles are then propagated to Earth, where their velocity distribution is recorded. The resulting SRDM differential flux on Earth in units of $(\mathrm{km/s})^{-1}\mathrm{cm}^{-2}\mathrm{s}^{-1}$ is given by

$$\frac{d\Phi_\odot}{dv_\chi} = \frac{1}{4\pi l^2} \frac{N_\mathrm{refl}}{N_\mathrm{sim}} \Gamma(m_\chi) f_\odot(v_\chi), \qquad (1)$$

where $l = 1 \, \mathrm{AU}$ is the distance between Earth and the Sun, $N_\mathrm{sim} = 10^5$ is the total number of simulated DM trajectories, N_refl is the number of simulated events with at least one scattering in the Sun, $\Gamma(m_\chi)$ represents the total rate of halo DM particles of mass m_χ falling into the Sun in the simulation, and $f_\odot(v_\chi)$ denotes the probability density function of the SRDM speed on Earth v_χ, as obtained from simulation.

The leading source of systematic uncertainty arises from the choice of atomic form factors in the calculation of DM-electron scattering rates, which affects both the SRDM and standard halo DM analyses. In this work, we use DaMaSCUS-SUN, which employs xenon atomic response functions from Ref. [26]. We adopt the Standard Solar Model (AGSS09) for this analysis [27, 28]. Although various solar models exist in the literature, the solar reflection results are only weakly sensitive to this choice [23].

We neglect attenuation of the SRDM flux due to the Earth's overburden as it is negligible at the DM-electron cross sections considered in this work. The extent of attenuation is model dependent, with nuclear recoil (NR) interactions producing stronger suppression than ER interactions. Even under the conservative assumption of equal contributions from ER and NR interactions, the critical DM-electron cross section above which the Earth's attenuation matters is $\sim 10^{-31} \, \mathrm{cm}^2$ for a $10 \, \mathrm{MeV}/c^2$ DM. This critical DM-electron cross section is larger for lighter DM [29]. In this work, we consider DM masses up to $10 \, \mathrm{MeV}/c^2$ and cross sections in the $10^{-39} \, \mathrm{cm}^2 - 10^{-35} \, \mathrm{cm}^2$ range, where overburden effects are safely negligible.

The resulting SRDM differential flux observed in a terrestrial detector is shown in Fig. 1 as a function of DM speed in the Earth's lab frame. A larger DM-electron
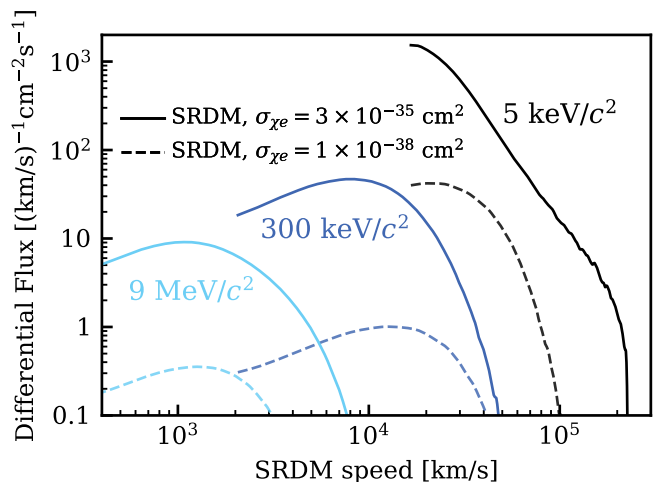

FIG. 1. SRDM differential flux in a terrestrial detector as a function of SRDM speed, computed via Monte Carlo simulations [25]. The shape of the differential flux depends on the DM mass (indicated by colors) and also the DM-electron cross section (indicated by line styles). The differential fluxes are computed to the lowest DM speed that can produce detectable signals in the detector for the given SRDM mass.

scattering cross section generally leads to a higher interaction rate in the detector, as DM is more likely to scatter with electrons in the liquid xenon target. It also increases the probability of DM reflection in the Sun, increasing the boost in velocity the DM particle receives. However, a sufficiently large DM-electron cross section can prevent DM from reaching the solar core, where hotter electrons provide even more substantial velocity boosts.

Datasets — We briefly describe the relevant features of the XENON1T and XENONnT datasets used in this analysis, further details are provided in Refs. [24] and [16] respectively.

XENON1T S2-only dataset: Both S1 and S2 signals in a liquid xenon TPC are measured in photoelectrons

(PE), with S2 signals typically two orders of magnitude larger in size than S1 signals. DM searches that require coincidence between S1 and S2 signals for event reconstruction have limited sensitivity to DM masses above approximately $3\,\mathrm{GeV}/c^2$, as lower-mass DM interactions often produce S1 signals below the detection threshold [3–5, 30]. Removing the S1 requirement and using only the S2 signal lowers the detection threshold further, extending sensitivity to lower mass DM. In this analysis, we use the data and associated resources from the XENON1T S2-only data release [24, 31].

A total of 30% of the dataset, corresponding to 77.5 live-days from XENON1T Science Run 1 [32], is used to optimize event selection criteria. The remaining 70%, comprising 180.7 live-days, is reserved for the final science search. The region of interest (ROI) is defined in terms of the S2 signal size, limited to S2 peaks within the range of $[150, 3000]$ PE, which corresponds to $0.2\,\mathrm{keV} - 3.7\,\mathrm{keV}$ in ER energies [24]. The region below 150 PE is excluded due to contamination from pileup and single-electron signals following large S2s, which remain poorly understood [17, 24, 33]. We impose an upper bound of 3000 PE, as above this value, the ER background is a mixture of events with only S2 signals and those with both S1 and S2 signals. No validated background model exists for this mixture.

We apply the same event selection criteria as in Ref. [24] to the science search data, and 45 events remain in the ROI of $S2 \in [150, 3000]$ PE. The S2s of these events are indicated by the short vertical gray ticks in the upper panel of the top subplot in Fig. 2.

To obtain the SRDM differential event rate as a function of S2, referred to as the S2 spectrum, we apply an energy threshold of 50 eV to the deposited energy before using the detector response matrix provided in the data release to convert the differential rate as a function of deposited energy to a function of S2 signal. The resulting S2 spectra depend on both the DM mass and the DM-electron cross section. Selected spectra are shown in the top subplot of Fig. 2.

XENONnT low-energy ER dataset: Events in the XENONnT low-energy ER dataset are required to have a valid pairing of S1-S2, and three-fold tight coincidence for S1 signals [16]. While this requirement results in a higher detector threshold of $\sim 1\,\mathrm{keV}$ compared to the XENON1T S2-only dataset, the XENONnT low-energy ER dataset is substantially cleaner as the novel subsystems in XENONnT reduced the ER backgrounds by approximately a factor of five relative to XENON1T [16]. In addition, having both S1 and S2 signals provides sufficient information to suppress backgrounds that dominate in ionization-only analyses.

The first science run of XENONnT, conducted from 6 July to 10 November 2021, yielded a livetime of 97.1 days. With a fiducial mass of (4.37 ± 0.14) tonnes, the low-energy ER dataset yields an exposure of
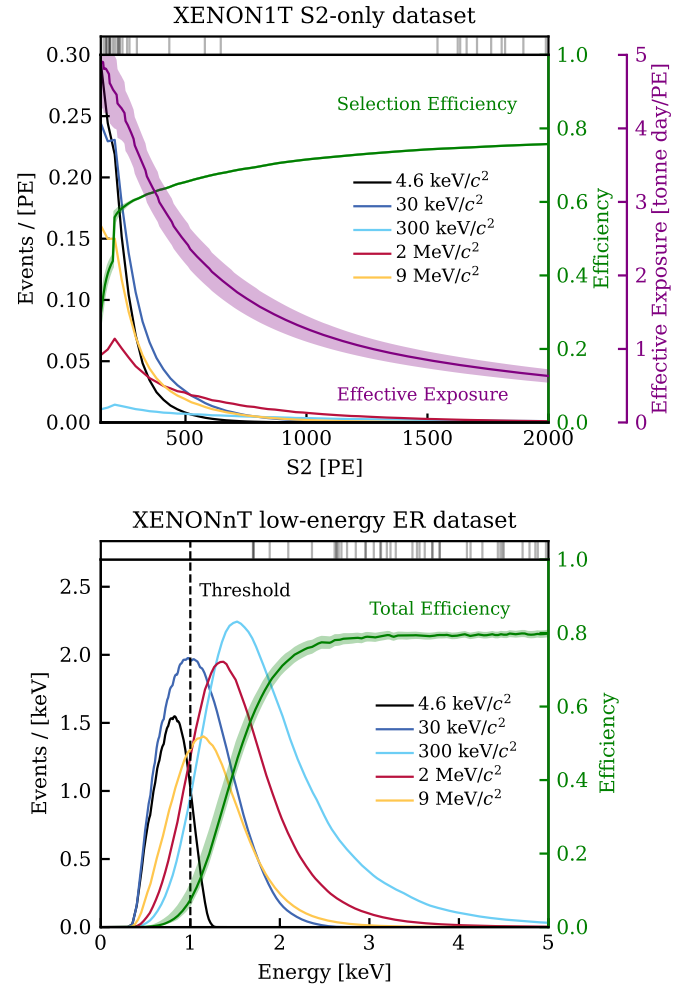

FIG. 2. Top: SRDM differential rates as a function of S2 area in the XENON1T detector evaluated at the 90% C.L. upper limits on the DM-electron cross section for the various SRDM masses (colors). Short vertical gray ticks in the narrow top panel indicate events in the XENON1T S2-only science search dataset. Green line (shaded band) shows the event-selection efficiencies (1σ uncertainty). Purple line (shaded band) shows the effective remaining exposure (1σ uncertainty) after selections. Bottom: SRDM differential rates as a function of reconstructed energy in the XENONnT detector evaluated at the 90% C.L. confidence interval on the DM-electron cross section for the various SRDM masses (colors). Short vertical gray ticks in the narrow top panel indicate events in the XENONnT low-energy ER dataset. Dashed vertical line indicates the 1 keV threshold. Green line (shaded band) shows the combined detection and event-selection efficiencies (1σ uncertainty) of the dataset.

1.16 tonne-years [16]. The analysis is performed in reconstructed energy with an ROI spanning 1–140 keV. Although the SRDM signal diminishes above 5 keV (see Fig. 2, bottom), the ROI is extended to 140 keV to constrain the flat background components more effectively.

We apply the same event selection criteria as in

Ref. [16]. The remaining 3658 events are indicated by short vertical gray ticks at their reconstructed energies in the upper panel of the bottom subplot in Fig. 2.

To obtain the SRDM differential rate in reconstructed energy, we convolve the true recoil spectrum with the detector response, incorporating both energy resolution, modeled using a skewed Gaussian, and the total efficiency, which is primarily determined by the S1 three-fold coincidence requirement and waveform-dependent reconstruction effects [9].

Accidental coincidence (AC) events, formed by the random pairing of uncorrelated S1 and S2 signals into spurious events, contribute to the background and are removed by the AC cut. We also apply selection acceptances, including the 500 PE S2 threshold and data quality cuts. The resulting signal spectra, which incorporate all detector and selection effects, are shown in the bottom subplot of Fig. 2.

The signal expectation peaks for a $300 \, \mathrm{keV}/c^2$ SRDM, as shown by the light blue curve in the bottom subplot of Fig. 2, where the solar upscattering is most efficient for DM masses comparable to the electron mass. DM models with lower masses are suppressed by the detection efficiency and selection acceptances of the XENONnT low-energy ER dataset, while those with higher masses are suppressed by the reduced local DM number density.

We adopt the same background model and associated constraints for the XENONnT low-energy ER dataset as in Ref.[16]. The energy spectra of the various background components included in this model are shown in Fig.3. The dominant contribution to the low-energy background
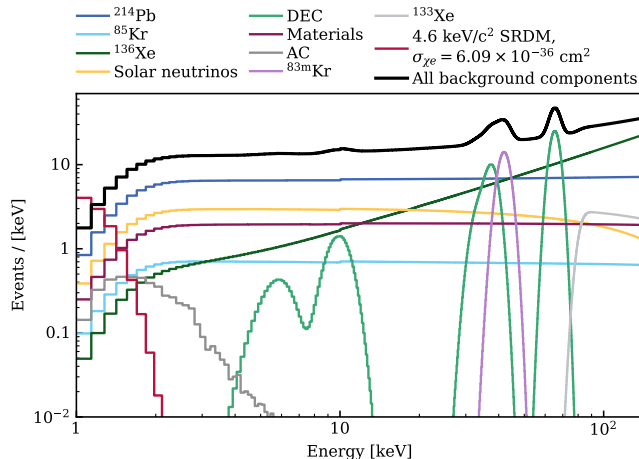

FIG. 3. Event expectation for the various background components in the XENONnT low-energy ER dataset. The spectrum of a $4.6 \, \mathrm{keV}/c^2$ SRDM signal with DM-electron cross section of $6.09 \times 10^{-36} \, \mathrm{cm}^2$ (unconstrained 90% C.L. confidence interval) is also shown for reference.

arises from the beta decay of ^{214}Pb, a progeny of the primordial ^{238}U decay chain, followed by ERs induced by

solar neutrino scattering. Additional background components include AC events, and gamma rays from radioactive decays in materials surrounding the detector and the beta decay of anthropogenic ^{85}Kr. Intrinsic radioactivity within the liquid xenon target introduces contributions from the two-neutrino double beta decay of ^{136}Xe and the double-electron capture (DEC) of ^{124}Xe. Residual contamination from prior calibration activities includes ^{83m}Kr and ^{133}Xe, the latter produced through neutron activation during ^{241}AmBe calibration campaigns conducted a few months before the start of the Science Run.

Statistical analysis — Due to the lack of a complete background model for the XENON1T S2-only dataset, we employ Yellin's optimal interval method with the P_{Max} test statistic [34] to set upper limits on the DM-electron scattering cross section, using the S2 area as the observable. The statistical trial factor associated with testing multiple intervals is taken into account using Monte Carlo simulations [35].

In contrast, for the XENONnT low-energy ER dataset, where a full background model is available, we employ an unbinned likelihood analysis over the reconstructed energy range from 1 to $140 \, \mathrm{keV}$. As in Ref. [16], the confidence intervals on the DM-electron scattering cross section for the various DM mass hypotheses are derived using the Feldman-Cousins unified interval construction with the profile likelihood ratio as the test statistic, assuming its asymptotic distribution of a χ^2 distribution with one degree of freedom [36–38]. To account for systematic uncertainties in the detection efficiency near the energy threshold, specifically for energies below $5 \, \mathrm{keV}$, we introduce a shape nuisance parameter that allows the efficiency curve to vary.

For DM models in which the DM-electron cross section affects only the total event rate, the confidence interval on the rate multiplier is computed for a fixed reference DM-electron cross section and subsequently translated into a confidence interval on the DM-electron cross section based on the reference DM-electron cross section. In contrast, for the SRDM signal model, the DM-electron cross section influences both the spectral shape and normalization. To handle degeneracy between the shape and normalization, we fix the rate multiplier and treat the DM-electron cross section purely as a shape parameter.

Results — Fig. 4 shows the 90% C.L. confidence intervals on the DM-electron cross section obtained from the XENON1T S2-only and XENONnT low-energy ER datasets. Existing constraints include those XENONnT Few Electrons analysis [17], other direct DM detection experiments [39, 40], and theoretical recasts XENON1T data [23, 41]. The previous theoretical recast using XENON1T S2-only data [23] employed an emission model in which the electron-yield summation was terminated too early, resulting in an underestimation of the signal expectation and consequently to weaker limits.

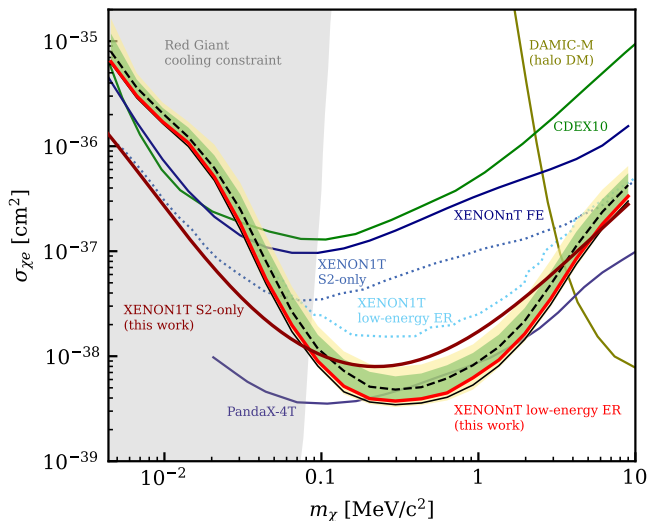No sensitivity band is shown for the XENON1T re-

FIG. 4. The dark red line shows the 90% C.L. upper limits on the DM-electron cross section using the XENON1T S2-only dataset. Due to the lack of a full background model for this dataset, Yellin's optimal interval method is used [34] and no sensitivity band can be constructed. The red line shows the 90% C.L. confidence intervals using the XENONnT low-energy ER dataset after applying the power constraint. Thin solid black line shows the 90% C.L. confidence intervals computed using only the XENONnT low-energy ER dataset without power constraint, while the dashed black line, along with the green and yellow bands, indicate the median expected sensitivity and the corresponding 1σ and 2σ bands respectively. We also show results from XENONnT Few Electrons (FE) analysis [17], PandaX [39], CDEX10 [40], and theoretical recasts of limits using XENON1T datasets [23, 41] in dotted. The gray shaded region at low DM mass indicates the parameter space excluded by stellar cooling constraints from red giants [42].

sult due to the lack of a full background model. For the XENONnT dataset, the median sensitivity along with the 1σ and 2σ bands are shown. The power-constrained 90% C.L. confidence interval is obtained by restricting any underfluctuation to at most -1σ [37]. Without the power constraint, the 90% C.L. confidence intervals obtained from the XENONnT low-energy ER dataset lies between -2 and -1σ of the sensitivity band and for all mass hypotheses. This underfluctuation originates from the absence of events between the detector threshold of $1\,\mathrm{keV}$ and the lowest observed event at $1.7\,\mathrm{keV}$ which is a region with high signal expectation. The absence of events in this region resulted in confidence intervals on the DM-electron cross section that are stronger than expected, consistent with a statistical fluctuation. The best-fit value of the efficiency shape parameter is approximately -0.31 for all mass hypotheses. This is within the allowed range of $[-2, 2]$ and consistent with the nominal value within uncertainties determined by simulations that consider variations in signal waveform, pileup and trigger behavior.

Using the XENONnT low-energy ER dataset, we set the most stringent confidence intervals on the DM-electron scattering cross section in the mass range from $0.2\,\mathrm{MeV}/c^2$ to $2\,\mathrm{MeV}/c^2$. In addition, the 90% C.L. upper limits derived from the XENON1T S2-only dataset exclude previously unconstrained DM-electron cross section in the lower mass range of $4.6\,\mathrm{keV}/c^2$ to $20\,\mathrm{keV}/c^2$. Although this region is already in tension with stellar cooling bounds from red giant (RG) observations [42], we include it here as the constraints from RG cooling and direct detection experiments are complementary and rely on different assumptions and systematics.

Summary and outlook — Sub-GeV dark matter in the SHM is typically too light to yield detectable signals in liquid xenon TPCs. However, upscattering of these DM particles from a variety of astrophysical objects can boost their velocity, making detection possible. In particular, the SRDM model considers DM scattering off electrons in the Sun, extending the sensitivity of liquid xenon TPCs to the keV–MeV mass regime.

In this work, we present novel 90% C.L. confidence intervals on the DM-electron scattering cross section. In the mass range between $4.6\,\mathrm{keV}/c^2$ and $20\,\mathrm{keV}/c^2$, and between $0.2\,\mathrm{MeV}/c^2$ and $2\,\mathrm{MeV}/c^2$, we exclude previously unconstrained parameter space, reaching a minimum of $3.41 \times 10^{-39}\,\mathrm{cm}^2$ for a mass of $0.3\,\mathrm{MeV}/c^2$ at 90% confidence level by considering SRDM models interacting via a heavy mediator. This extension of sensitivity to lower masses is achieved by considering the upscattering of DM in the Sun, without assuming any new interactions.

Future developments will focus on improving the efficiency of the Monte Carlo calculation of the solar-reflected DM flux at very low DM-electron cross sections, where scattering becomes rare and event generation becomes computationally expensive. The XENONnT experiment continues to collect data under improved detector conditions, including ongoing efforts to suppress backgrounds from photoionizing impurities, which are expected to lower the accidental coincidence background rate and enhance sensitivity to sub-GeV dark matter.

---

* conrad@fysik.su.se
† Also at INFN-Roma Tre, 00146 Roma, Italy
‡ Now at Department of Physics & Astronomy, Bucknell University, Lewisburg, PA, USA
§ Also at Coimbra Polytechnic - ISEC, 3030-199 Coimbra, Portugal
¶ plt2120@columbia.edu
** xenon@lngs.infn.it

[1] G. Bertone, D. Hooper, and J. Silk, Particle dark matter: Evidence, candidates and constraints, Phys. Rept. **405**, 279 (2005), arXiv:hep-ph/0404175.

[2] L. Roszkowski, E. M. Sessolo, and S. Trojanowski, WIMP dark matter candidates and searches—current status and future prospects, Rept. Prog. Phys. **81**, 066201 (2018), arXiv:1707.06277 [hep-ph].

[3] E. Aprile *et al.* (XENON Collaboration), WIMP Dark Matter Search Using a 3.1 Tonne-Year Exposure of the XENONnT Experiment, Phys. Rev. Lett. **135**, 221003 (2025), arXiv:2502.18005 [hep-ex].

[4] J. Aalbers *et al.* (LZ Collaboration), Dark Matter Search Results from 4.2 Tonne-Years of Exposure of the LUX-ZEPLIN (LZ) Experiment, Phys. Rev. Lett. **135**, 011802 (2025), arXiv:2410.17036 [hep-ex].

[5] Z. Bo *et al.* (PandaX Collaboration), Dark Matter Search Results from 1.54 Tonne·Year Exposure of PandaX-4T, Phys. Rev. Lett. **134**, 011805 (2025), arXiv:2408.00664 [hep-ex].

[6] E. Aprile *et al.* (XENON Collaboration), The XENON1T Dark Matter Experiment, Eur. Phys. J. C **77**, 881 (2017), arXiv:1708.07051 [astro-ph.IM].

[7] E. Aprile *et al.* (XENON Collaboration), Conceptual design and simulation of a water Cherenkov muon veto for the XENON1T experiment, JINST **9**, P11006, arXiv:1406.2374 [astro-ph.IM].

[8] E. Aprile *et al.* (XENON Collaboration), The neu-tron veto of the XENONnT experiment: Results with demineralized water, Eur. Phys. J. C **85**, 695 (2025), arXiv:2412.05264 [physics.ins-det].

[9] E. Aprile *et al.* (XENON Collaboration), XENONnT analysis: Signal reconstruction, calibration, and event selection, Phys. Rev. D **111**, 062006 (2025), arXiv:2409.08778 [hep-ex].

[10] E. Aprile *et al.* (XENON Collaboration), The XENONnT dark matter experiment, Eur. Phys. J. C **84**, 784 (2024), arXiv:2402.10446 [physics.ins-det].

[11] G. Plante, E. Aprile, J. Howlett, and Y. Zhang, Liquid-phase purification for multi-tonne xenon detectors, Eur. Phys. J. C **82**, 860 (2022), arXiv:2205.07336 [physics.ins-det].

[12] M. Murra, D. Schulte, C. Huhmann, and C. Weinheimer, Design, construction and commissioning of a high-flow radon removal system for XENONnT, Eur. Phys. J. C **82**, 1104 (2022), arXiv:2205.11492 [physics.ins-det].

[13] K. Fujii, Y. Endo, Y. Torigoe, S. Nakamura, T. Haruyama, K. Kasami, S. Mihara, K. Saito, S. Sasaki, and H. Tawara, High-accuracy measurement of the emission spectrum of liquid xenon in the vacuum ultraviolet region, Nuclear Instruments and Methods in Physics Research Section A: Accelerators, Spectrometers, Detectors and Associated Equipment **795**, 293 (2015).

[14] A. Lansiart, A. Seigneur, J.-L. Moretti, and J.-P. Morucci, Development research on a highly luminous condensed xenon scintillator, Nucl. Instrum. Methods **135**, 47–52 (1976).

[15] N. W. Evans, C. A. J. O'Hare, and C. McCabe, Refinement of the standard halo model for dark matter searches in light of the Gaia Sausage, Phys. Rev. D **99**, 023012 (2019), arXiv:1810.11468 [astro-ph.GA].

[16] E. Aprile *et al.* (XENON Collaboration), Search for New Physics in Electronic Recoil Data from XENONnT, Phys. Rev. Lett. **129**, 161805 (2022), arXiv:2207.11330 [hep-ex].

[17] E. Aprile *et al.* (XENON Collaboration), Search for Light Dark Matter in Low-Energy Ionization Signals from XENONnT, Phys. Rev. Lett. **134**, 161004 (2025), arXiv:2411.15289 [hep-ex].

[18] T. Bringmann and M. Pospelov, Novel direct detection constraints on light dark matter, Phys. Rev. Lett. **122**, 171801 (2019), arXiv:1810.10543 [hep-ph].

[19] J.-W. Wang, A. Granelli, and P. Ullio, Direct Detection Constraints on Blazar-Boosted Dark Matter, Phys. Rev. Lett. **128**, 221104 (2022), arXiv:2111.13644 [astro-ph.HE].

[20] A. Das and M. Sen, Boosted dark matter from diffuse supernova neutrinos, Phys. Rev. D **104**, 075029 (2021), arXiv:2104.00027 [hep-ph].

[21] T. Emken, C. Kouvaris, and N. G. Nielsen, The Sun as a sub-GeV Dark Matter Accelerator, Phys. Rev. D **97**, 063007 (2018), arXiv:1709.06573 [hep-ph].

[22] H. An, M. Pospelov, J. Pradler, and A. Ritz, Directly Detecting MeV-scale Dark Matter via Solar Reflection, Phys. Rev. Lett. **120**, 141801 (2018), [Erratum: Phys.Rev.Lett. 121, 259903 (2018)], arXiv:1708.03642 [hep-ph].

[23] T. Emken, Solar reflection of light dark matter with heavy mediators, Phys. Rev. D **105**, 063020 (2022), arXiv:2102.12483 [hep-ph].

[24] E. Aprile *et al.* (XENON Collaboration), Light Dark Matter Search with Ionization Signals in XENON1T,

Phys. Rev. Lett. **123**, 251801 (2019), arXiv:1907.11485 [hep-ex].

[25] T. Emken, Dark Matter Simulation Code for Underground Scatterings - Sun Edition (DaMaSCUS-SUN) [Code, v0.1.1], Astrophysics Source Code Library record [ascl:2102.018]. The code can be found under `https://github.com/temken/damascus-sun`. Version 1.0.0 is archived as DOI:10.5281/zenodo.10948125 (2021).

[26] R. Catena, T. Emken, N. A. Spaldin, and W. Tarantino, Atomic responses to general dark matter-electron interactions, Phys. Rev. Res. **2**, 033195 (2020), [Erratum: Phys.Rev.Res. 7, 019001 (2025)], arXiv:1912.08204 [hep-ph].

[27] A. Serenelli, S. Basu, J. W. Ferguson, and M. Asplund, New Solar Composition: The Problem With Solar Models Revisited, Astrophys. J. Lett. **705**, L123 (2009), arXiv:0909.2668 [astro-ph.SR].

[28] M. Asplund, N. Grevesse, A. J. Sauval, and P. Scott, The chemical composition of the sun, Annual Review of Astronomy and Astrophysics **47**, 481 (2009).

[29] M. Crisler, R. Essig, J. Estrada, G. Fernandez, J. Tiffenberg, M. Sofo haro, T. Volansky, and T.-T. Yu (SENSEI Collaboration), SENSEI: First Direct-Detection Constraints on sub-GeV Dark Matter from a Surface Run, Phys. Rev. Lett. **121**, 061803 (2018), arXiv:1804.00088 [hep-ex].

[30] E. Aprile *et al.* (XENON Collaboration), First Search for Light Dark Matter in the Neutrino Fog with XENONnT, Phys. Rev. Lett. **134**, 111802 (2025), arXiv:2409.17868 [hep-ex].

[31] E. Aprile *et al.* (XENON Collaboration), XENON1T S2-only data release (2020), `https://github.com/XENON1T/s2only_data_release`.

[32] E. Aprile *et al.* (XENON Collaboration), Dark Matter Search Results from a One Ton-Year Exposure of XENON1T, Phys. Rev. Lett. **121**, 111302 (2018), arXiv:1805.12562 [astro-ph.CO].

[33] E. Aprile *et al.* (XENON Collaboration), Emission of single and few electrons in XENON1T and limits on light dark matter, Phys. Rev. D **106**, 022001 (2022), [Erratum: Phys.Rev.D 110, 109903 (2024)], arXiv:2112.12116 [hep-ex].

[34] S. Yellin, Finding an upper limit in the presence of an unknown background, Phys. Rev. D **66**, 032005 (2002).

[35] P. L. Tan, yellinpmax: Python package to compute yellin's optimal interval with pmax test statistic (2024).

[36] G. J. Feldman and R. D. Cousins, A Unified approach to the classical statistical analysis of small signals, Phys. Rev. D **57**, 3873 (1998), arXiv:physics/9711021.

[37] D. Baxter *et al.*, Recommended conventions for reporting results from direct dark matter searches, Eur. Phys. J. C **81**, 907 (2021), arXiv:2105.00599 [hep-ex].

[38] S. S. Wilks, The Large-Sample Distribution of the Likelihood Ratio for Testing Composite Hypotheses, Annals Math. Statist. **9**, 60 (1938).

[39] G. Shen *et al.* (PandaX Collaboration), Search for Solar Boosted Dark Matter Particles at the PandaX-4T Experiment, Phys. Rev. Lett. **134**, 161003 (2025), arXiv:2412.19970 [hep-ex].

[40] Z. Y. Zhang *et al.* (CDEX Collaboration), Experimental Limits on Solar Reflected Dark Matter with a New Approach on Accelerated-Dark-Matter–Electron Analysis in Semiconductors, Phys. Rev. Lett. **132**, 171001 (2024), arXiv:2309.14982 [hep-ex].

[41] H. An, H. Nie, M. Pospelov, J. Pradler, and A. Ritz, Solar reflection of dark matter, Phys. Rev. D **104**, 103026 (2021).

[42] J. H. Chang, R. Essig, and A. Reinert, Light(ly)-coupled dark matter in the kev range: freeze-in and constraints, Journal of High Energy Physics **2021**, 10.1007/jhep03(2021)141 (2021).